Materials Chemistry and Physics 304 (2023) 127838

Contents lists available at ScienceDirect

Materials Chemistry and Physics

journal homepage: www.elsevier.com/locate/matchemphys

Effects of bovine serum albumin on the corrosion behavior of biodegradable Zn–Cu alloy under dynamic flowing conditions

Xin Zhang [a,b], Lu Zhang [a,b], Dekang Zhang [a,b], Linyuan Han [a,b,**], Jing Bai [a,b], Zhihai Huang [a,b], Chao Guo [a,b], Feng Xue [a,b], Paul K. Chu [c], Chenglin Chu [a,b,*]

[a] School of Materials Science and Engineering, Southeast University, Nanjing, 211189, Jiangsu, China
[b] Jiangsu Key Laboratory for Advanced Metallic Materials, Southeast University, Nanjing, 211189, China
[c] Department of Physics, Department of Materials Science and Engineering, and Department of Biomedical Engineering, City University of Hong Kong, Hong Kong, China

HIGHLIGHTS

- A general linear model between corrosion rates of Zn–Cu alloy and BSA concentrations of Hanks' solution was established.
- The corrosion properties of the Zn–Cu alloy under simulated flowing conditions were investigated.
- The addition of BSA promoted the uniformity of corrosion.
- BSA inhibited corrosion rates of Zn–Cu alloy but the inhibition effectiveness reduced as the BSA content increased.

ARTICLE INFO

Keywords:
Zn-Cu alloy
Bovine serum albumin
Corrosion mechanism
In vitro
Flowing conditions

ABSTRACT

In vitro experimental evaluation of biodegradable materials must consider the dynamic effects of body fluids and blood in the physiological environment, as biomedical implants are frequently in contact with body fluids and protein adsorption impacts the degradation process. However, little research has been done on the effects of proteins on the corrosion properties of zinc-based alloys under non-static conditions. Herein, the corrosion behavior of the Zn–Cu alloy in Hanks' solution under flowing conditions is examined in relation to the impacts of different bovine serum albumin (BSA) concentrations. Although BSA retards corrosion, the effects of smaller protein concentrations are more significant during the early stage of metal degradation. The corrosion rate of the Zn–Cu alloy decreases with BSA concentrations during immersion before stabilizing. Based on this, a numerical model for the corrosion process of Zn–Cu alloy under dynamic flowing conditions is established. Between the corrosion rates (*CR*) of Zn–Cu alloy and BSA concentrations (*CB*) of Hanks' solution matched a linear connection of the formula $CR = \alpha \bullet CB + \beta$. The results of this research have important significance for the development and application of biodegradable zinc-based biomedical implants.

1. Introduction

Demand for medical implants is increasing with the world's aging population and medical technology advances [1]. Biodegradable polymer implants have broad application prospects by taking the advantage of degradability, safety, and non-toxicity, such as medical sutures, bone nails, and drug release [2]. However, there are some problems with polymer implants, including mechanical stiffness and strength limitations, adverse tissue reactions, foreign body reactions, and delayed reactions of degraded tissue [3,4]. In comparison, biodegradable metals have better mechanical properties and good biocompatibility [5–8].

In recent years, zinc (Zn) and zinc-based alloys have become a research hotspot [9–11]. The standard electrode potential of Zn (−0.763 V) is between those of Mg (−2.372 V) and Fe (−0.447 V) and the degradation rate which is predicted to be appropriate theoretically has been confirmed by *in vivo* and *in vitro* experiments [12–14]. Furthermore, Zn is an essential element involved in almost all metabolic activities in the human body including cell proliferation as well as the

* Corresponding author. School of Materials Science and Engineering, Southeast University, Nanjing, 211189, Jiangsu, China.
** Corresponding author. School of Materials Science and Engineering, Southeast University, Nanjing, 211189, Jiangsu, China.
E-mail addresses: 101013242@seu.edu.cn (L. Han), clchu@seu.edu.cn (C. Chu).

https://doi.org/10.1016/j.matchemphys.2023.127838
Received 5 December 2022; Received in revised form 3 March 2023; Accepted 28 April 2023
Available online 29 April 2023
0254-0584/

immune and nervous systems. The corrosion products (ZnO, $Zn(OH)_2$, etc.) of Zn are also safe, non-toxic, and with high biocompatibility. Bowen et al. [15] have demonstrated that zinc may exhibit an anti-proliferative effect and protect against restenosis after stent implantation. Henning et al. [16] have found that Zn has good anti-atherosclerosis functions and the corrosion product of ZnO helps the formation of new blood vessels in tissue healing [17]. In addition to easier heat treatment and processing [18], Zn has a lower melting point (400 °C) and smaller reactivity than Mg. Moreover, zinc alloys are more radiopaque than magnesium alloys, making *in situ* monitoring during surgery easier [19].

However, the mechanical properties of pure zinc are poor and cannot meet the requirements of the human body and alloying is one of the effective methods to improve the properties. Common alloying elements include Mg, Al, Li, Ca, Sr, Ge, Ag, Mn, and Cu [20–25]. Copper (Cu) is another essential trace element for connective tissue development, nerve coverage, and bone growth [26]. Cu also promotes the proliferation of vascular endothelial cells to accelerate vascular reconstruction [27]. In fact, Cu deficiency can cause normal cell anemia, neuroticism, as well as abnormal metabolism of sugar and cholesterol. Furthermore, Cu has certain antibacterial properties that are helpful in mitigating infection after surgery [28,29]. Another practical way for preventing corrosion and enhancing performance is the use of different composite electrochemical coatings [30]. Tseluikin et al. [31]found that composite electrochemical coatings improved the corrosion stability of zinc–nickel alloy in 0.5 M H_2SO_4 solution. Shourgeshty et al. [32] have improved the wear resistance of low-carbon steel through electroplated functionally graded Zn–Ni–Al_2O_3 coatings by continuously changing the duty cycle/frequency.

Human blood and body fluids contain a myriad of proteins, organic acids, and inorganic electrolytes and the protein composition is quite complex. Albumin is one of the common proteins in the human body [33]. Proteins adsorption occurs and affects corrosion and degradation process of the materials when metallic implants contact body fluids [34]. Liu et al. [35] showed that pure Zn immersed in organic media for 168 h slowed degradation and rapid protein adsorption enhances the polarization resistance and amplifies local corrosion to alter degradation. Liu et al. [36] investigated that the effects of albumin on pure Zn in artificial plasma and the corrosion products consist of albumin and zinc oxide/zinc hydroxide. Despite recent developments, it is still unclear how protein adsorption affects the progression of corrosion in Zn alloys.

The majority of previous studies have focused on static immersion tests, whereas body fluids are constantly replenished and in motion in the body. Especially for degradable metals, the dynamic conditions may produce results different from those obtained observed from static immersion *in vitro* [37]. Hence, in this study, the effects of the bovine serum albumin (BSA) concentration on the corrosion properties of the Zn–Cu alloy under simulated fluid flow are investigated and the relationship between the corrosion rate and time is established. The findings are important for clinical adoption of biodegradable metals.

2. Materials and methods

2.1. Materials preparation

The Zn–Cu alloy selected for this study had a Cu concentration 0.10 ± 0.01 wt% and a Zn concentration 99.90 ± 0.01 wt%, which determined by the AXxLMF15 direct reading spectrometer. The alloy was cut into samples with dimensions of 60 mm × 15 mm × 2 mm, ground with #400, #600, #800, #1200, and #2000 silicon carbide (SiC) papers, and cleaned in ethanol and distilled water. An area of 1 × 1 cm^2 was exposed and the rest of the surface was covered by insulating tape and silicone rubber to avoid galvanic corrosion.

2.2. Immersion tests

The dynamic measurement platform is illustrated in Fig. 1. The sample was put on the bottom of the chamber and the liquid storage tank was placed in a constant temperature water bath (HH-1 digital constant temperature water bath) at 37 °C. The liquid medium in the tank had a volume of 2 L. A peristaltic pump (WT600CA high precision, 100–3000 ml min^{-1}) provided the liquid circulation by extracting the medium from the storage tank, injecting it into a catheter. The electrochemical impedance was monitored *in situ* in real time at different time. The flow quantity of immersion fluid was set as 200 ml min^{-1} corresponding to its average flow rate of 0.3 cm s^{-1}.

The Hanks' balanced salt solution was chosen as the immersion fluid and the composition is presented in Table 1. The concentration of BSA was set to be 1.7 g L^{-1}, 3.4 g L^{-1}, or 5.1 g L^{-1} and the solution pH was 7.40 ± 0.05 at 37 ± 0.5 °C. The fluid volume was 2000 ml and it was replenished at 24 h after the pH was recorded.

2.3. Materials and surface characterization

The surface morphology and microstructure of the Zn–Cu alloy samples after immersion were examined by field-emission scanning electron microscopy (FE-SEM, FEI, Sirion 200, USA) at 20 kV. The corrosion products produced on the surface were analyzed by X-ray diffraction (XRD, Bruker, D8-discover) employing Cu K_α ($\lambda = 1.54056$ Å) radiation in the 2θ range of 10–90° at a glancing angle of 0.02° and scanning rate of 0.15 s·step^{-1}. Fourier transform infrared spectrometry (FTIR, Nicolet iS10, USA, 400-4000 cm^{-1}) was employed the chemical structure and energy-dispersive X-ray spectroscopy (EDS, Oxford, UK) was utilized to determine the surface elemental composition. 50 μl of FITC (fluorescein isothiocyanate) was put on the sample and refrigerated at 4 °C for 12 h prior to laser confocal microscopy (CLSM, Nikon, A1RHD25, JPN) to monitor protein adsorption.

2.4. Electrochemical evaluation

Electrochemical impedance spectroscopy (EIS) was conducted on an electrochemical workstation (VersaSTAT 3 F) every 24 h. During the *in*

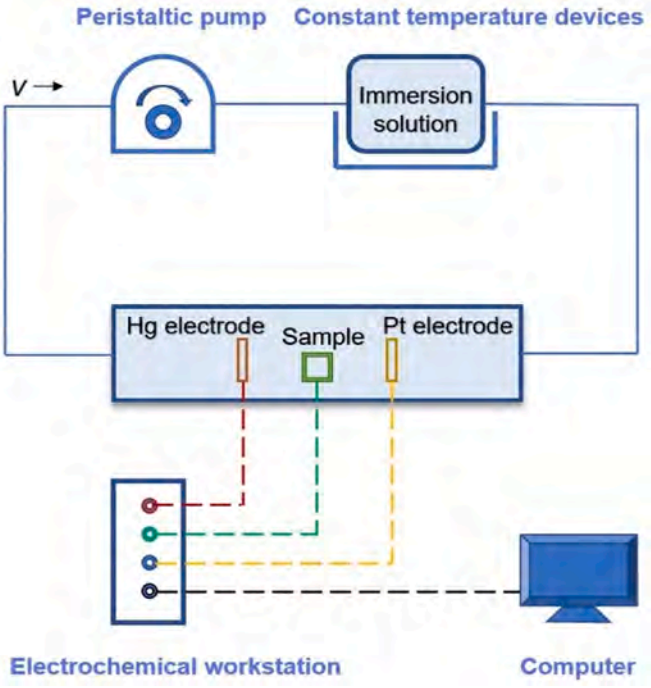

Fig. 1. Schematic of the dynamic test under flowing conditions.

Table 1
Chemical composition of Hanks' solution ($g{\cdot}L^{-1}$).

Reagents	NaCl	KCl	$MgSO_4{\cdot}7H_2O$	KH_2PO_4	$NaHCO_3$	$Na_2HPO_4{\cdot}H_2O$	$CaCl_2$	Glucose
Composition ($g{\cdot}L^{-1}$)	6.85	0.27	0.04	0.02	0.35	0.04	0.65	0.28

situ electrochemical tests, the dynamic flowing conditions were temporarily suspended and the open circuit test (OCT) was carried out to achieve steady state conditions. The reference, counter and working electrodes were the saturated calomel electrode (SCE), Pt electrode and sample, respectively. The frequencies were scanned from 100 kHz to 0.1 Hz and the potential amplitude was 0.01 V. Three parallel experiments were conducted and the impedance spectras were analyzed and fitted by the ZView software.

2.5. Statistical analysis

The data were analyzed and plotted using the Origin 8.5 software (Originlab Corporation, Wellesley Hills, USA). The data represented the average from three experiments and fitting was performed to estimate the correlation.

3. Results

3.1. Morphology and microstructure of the Zn–Cu samples after immersion

Fig. 2 shows the morphologies and elemental information of the corrosion products on the Zn–Cu samples which were immersed in Hanks' solution with different BSA concentrations for 120 h under the dynamic conditions. As shown in Fig. 2 (a), the samples gradually formed irregular granular corrosion products with nonuniform thickness which was immersed in the BSA-free Hanks' solution. According to the EDS maps, the primary substances on the surface are carbide, oxide, and hydroxide. C and O are irregularly distributed. The correlation between the Ca and P distributions suggests that the Ca–P phase has formed. Apart from a tiny number of granular corrosion products dispersed randomly on the surface, the corrosion products are short rods that equally cover the surface after the addition of 1.7 g L^{-1} BSA. Combined with EDS maps analysis, the oxide, hydroxide, and Ca–P phases and protein chelates are uniformly distributed on the surface of the samples, whereas the randomly distributed granular products are mainly carbide (Fig. 2 (b)). As the concentration of BSA goes up, the proportion of the short rod-shape corrosion product increases and the distribution becomes more uniform (Fig. 2 (c) and (d)). The results indicate that BSA leads to a more uniform corrosion of the alloy.

BSA adsorption on the surface of the samples was examined by laser confocal microscopy after immersion in Hanks' solution with BSA concentrations of 1.7 g L^{-1}, 3.4 g L^{-1}, and 5.1 g L^{-1}. The green fluorescence originates from the FITC-labeled BSA. When the concentration is 1.7 g L^{-1}, a small amount of BSA adsorbs locally onto the surface, and when the concentration is increased to 3.4 g L^{-1}, the fluorescence becomes more intense, indicating that BSA is present on the majority of the surface. BSA covers the surface and forms a thicker film when the concentration is raised to 5.1 g L^{-1},. The results indicate that the concentration of BSA affects adsorption, the fluorescence intensity increases gradually with the increase of BSA concentration in the solution, and the adsorption of protein also rises up accordingly.

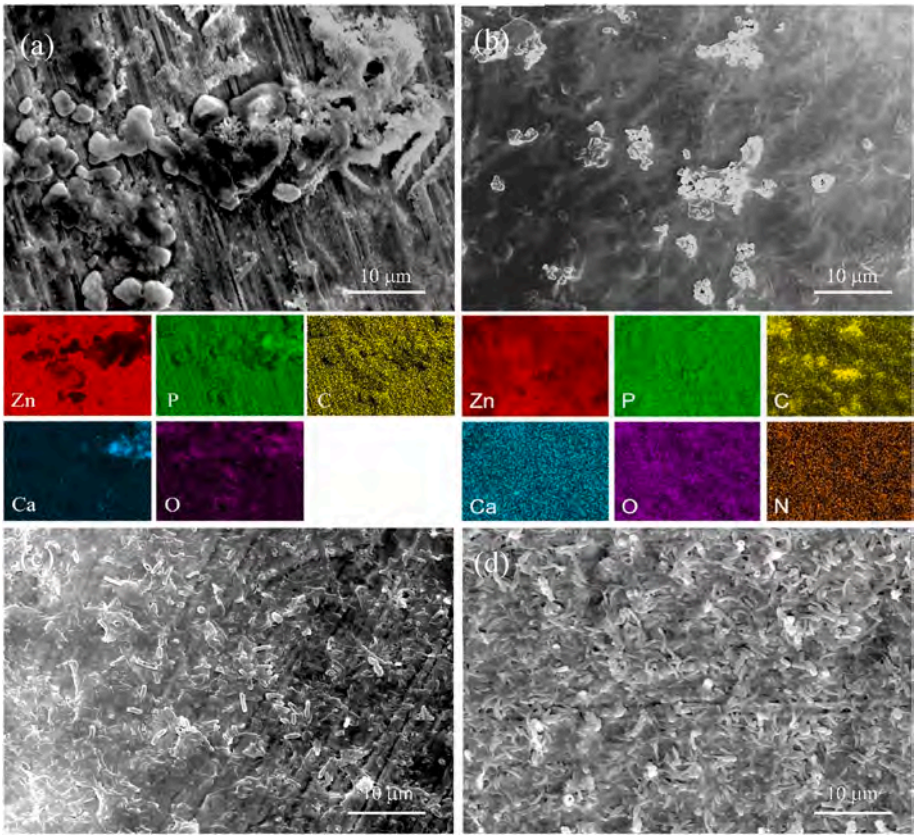

Fig. 2. Morphologies and EDS maps of the corrosion products on the Zn–Cu alloys immersed in Hanks' solutions with different BSA concentrations: (a) No BSA, (b) 1.7 g L^{-1} BSA, (c) 3.4 g L^{-1} BSA, and (d) 5.1 g L^{-1} BSA.

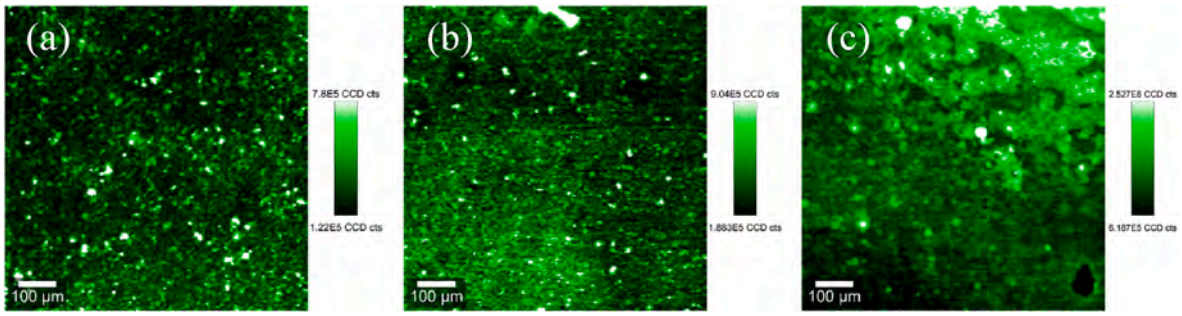

Fig. 3. Confocal fluorescence images showing adsorption of BSA on the Zn–Cu alloy in contact with different concentrations of BSA: (a) 1.7 g L^{-1} BSA, (b) 3.4 g L^{-1} BSA, and (c) 5.1 g L^{-1} BSA.

Figs. 4 and 5 depict the cross-sectional morphologies and corrosion product thickness after 120 h of immersion. The sample soaked in Hanks' solution has the thickest product layer with an average thickness of 5.19 ± 0.88 μm, but the thickness decreases when BSA was added. The average thickness of the corrosion product layer increases from 1.84 ± 0.48 μm to 3.26 ± 0.21 μm and the layer becomes more uniform with increasing BSA concentrations.

The line scans of the cross-section of the corrosion products after immersion in Hanks' solution with 1.7 g L^{-1} BSA are depicted in Fig. 6. The concentration of Ca, P and N increased slightly at the beginning and then decreased, whereas the concentration of C and O increased with the decrease of Zn concentration. It can be explained that the Ca–P phase and protein are preferentially deposited on the surface to form the inner layer of the corrosion products, while carbide, oxide, and hydroxide are deposited on the outer layer subsequently.

After immersion in Hanks' solution with different BSA concentrations for 120 h, the surface was analyzed by XRD and the results are shown in Fig. 7 (a). There is no significant difference among the different samples and the surface is mainly composed of ZnO and Zn.

As shown in Fig. 7 (b), the FTIR spectra in reveal amide I (double bond CO) of BSA at 1640 cm^{-1} and the peak shift indicates that Zn^{2+} binds with the BSA carbonyl group. The peak at 1540 cm^{-1} is attributed to amide II (NH bending and C–N stretching) of CONH and the absence of the BSA amide II peak at 1540 cm^{-1} suggests that Zn^{2+} binds with the

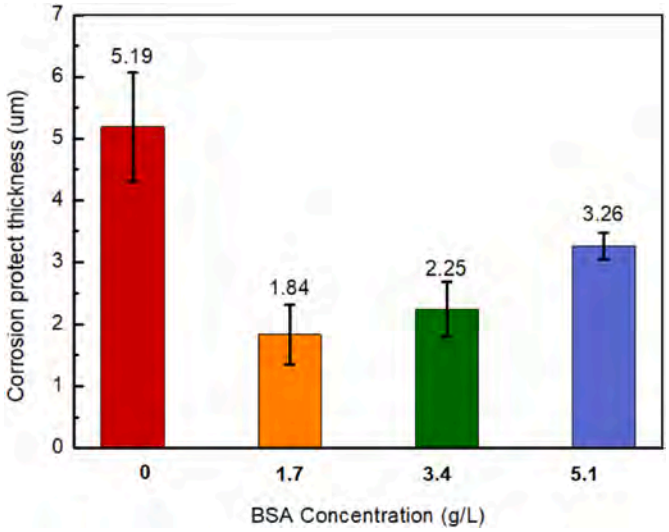

Fig. 5. Thickness of the corrosion products on the Zn–Cu alloy soaked in Hanks' solution containing different concentrations of BSA.

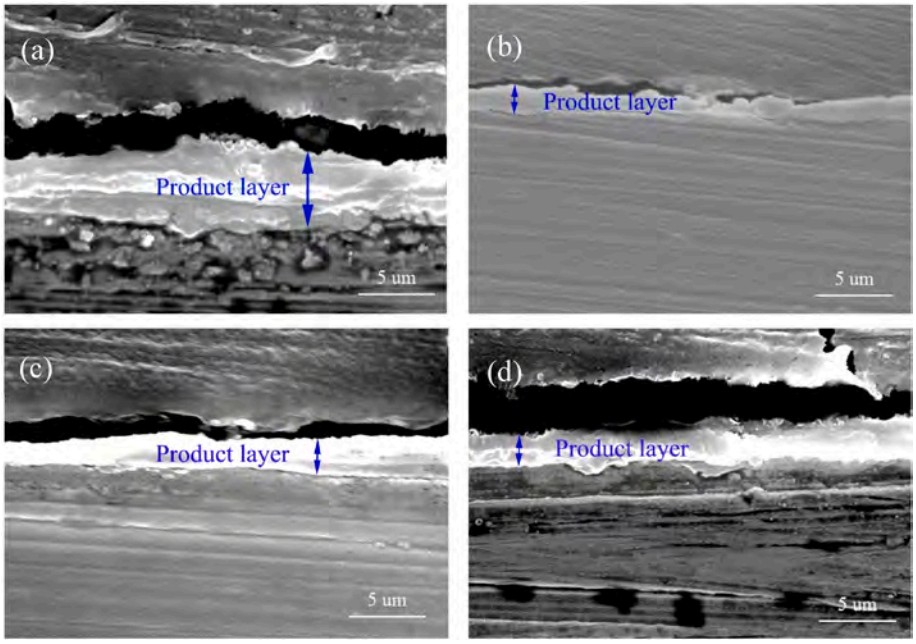

Fig. 4. Cross-sectional morphology of the corrosion products on the Zn–Cu alloy in contact with different concentrations of BSA: (a) No BSA, (b) 1.7 g L^{-1} BSA, (c) 3.4 g L^{-1} BSA, and (d) 5.1 g L^{-1} BSA.

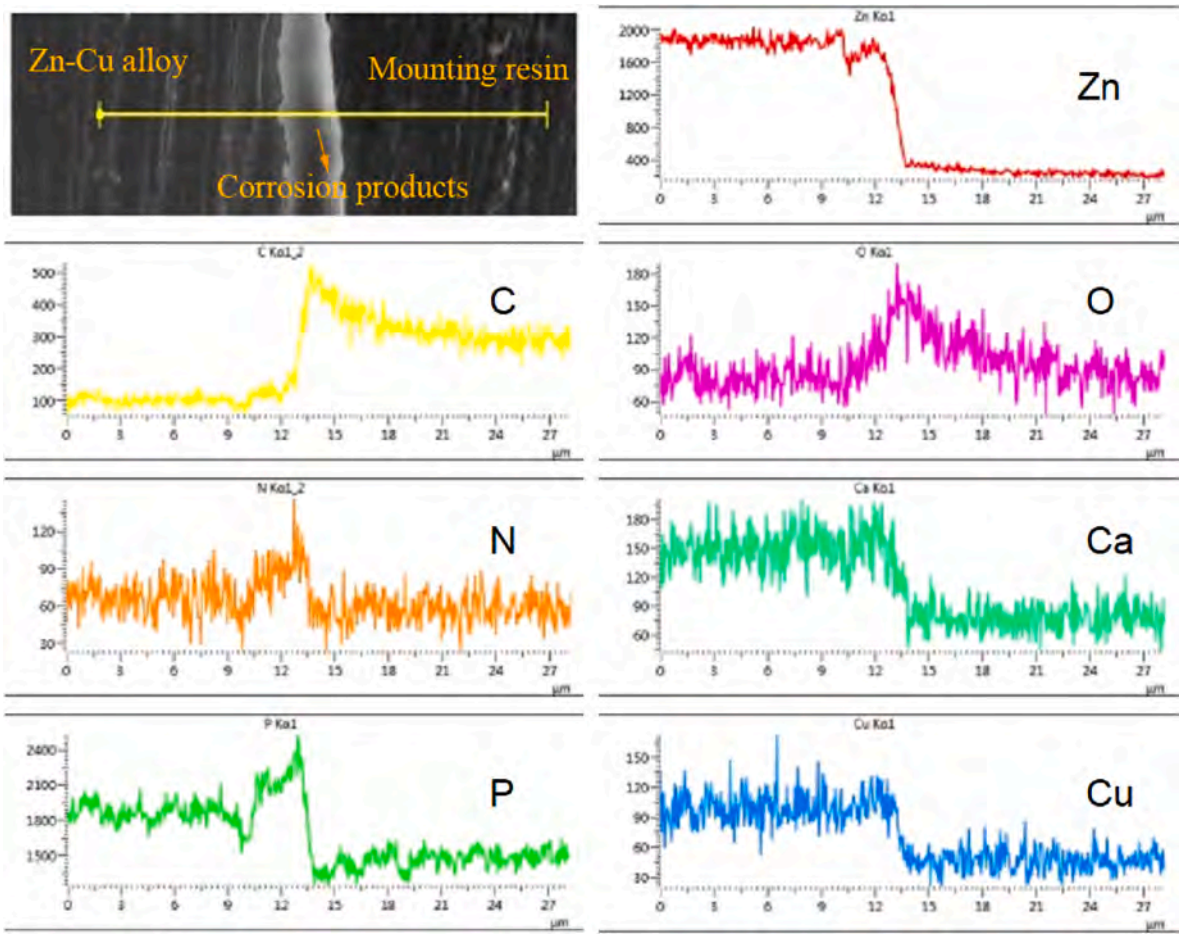

Fig. 6. Line scans of cross sections of corrosion products on the Zn–Cu alloy immersed in Hanks' solution containing 1.7 g L^{-1} BSA.

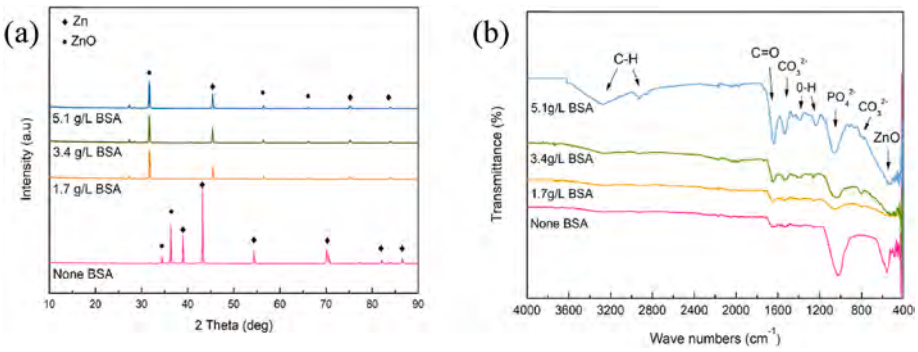

Fig. 7. (a) XRD spectra and (b) FTIR spectra of the Zn–Cu alloy immersed in Hanks' solution containing different concentrations of BSA for 120 h.

C–N group as well. The peaks at 2920 cm^{-1} and 3280 cm^{-1} corresponding to stretching of C–H in BSA. The intensity of the amide II peak and C–N is higher for larger BSA concentration due to accumulation of BSA on the surface. The peak at 553 cm^{-1} is related to ZnO, and the PO_4^{3-} peak appears at 1060 cm^{-1}. The wide band around 802 cm^{-1} arises from CO_3^{2-}. The results suggest that the degradation products comprise primarily zinc oxide, zinc phosphate, zinc carbonate, and BSA chelates.

To better analyze the chemical composition of corrosion products, XPS was carried out on the Zn–Cu alloy after immersion for 120 h. As shown in Fig. 8(a), elements Zn, O, C, Ca and P appeared in the survey spectra of all samples. Element N appeared when Hanks' solution added BSA, and the N 1 s peak was detected at 400.0 eV in the spectrum. As shown in Fig. 9(b–d), the curve fits of Zn 2p, C 1s 2p and P 2p are displayed after deconvolution. In high-resolution XPS spectra of Zn 2p, there were two single peaks, Zn 2p 1/2 and Zn 2p 3/2, respectively. Referring to the database of binding energy, the peak at 1022.5eV was attributed to $ZnCO_3$. The peaks located at 1021.2–1022.5eV suggested the existence of ZnO and $Zn(OH)_2$. The C 1s spectrum was displayed in Fig. 3(c), the samples with no BSA showed the peaks of C–O (ca. 286.4 eV) and C–C/C–H (ca. 284.8 eV). When Hanks' solution added 1.7 g L^{-1} BSA, the peaks of C 1s had one more sub-peak of C═O (ca. 287.7 eV). The P 2p spectra consisting of one single peak was located at 133.4–133.9 eV, which belongs to PO_4^{3-}, indicating that corrosion products included phosphate compounds. Therefore, after 120 h of immersion in Hanks' solution, the corrosion products were ZnO, $Zn(OH)_2$,

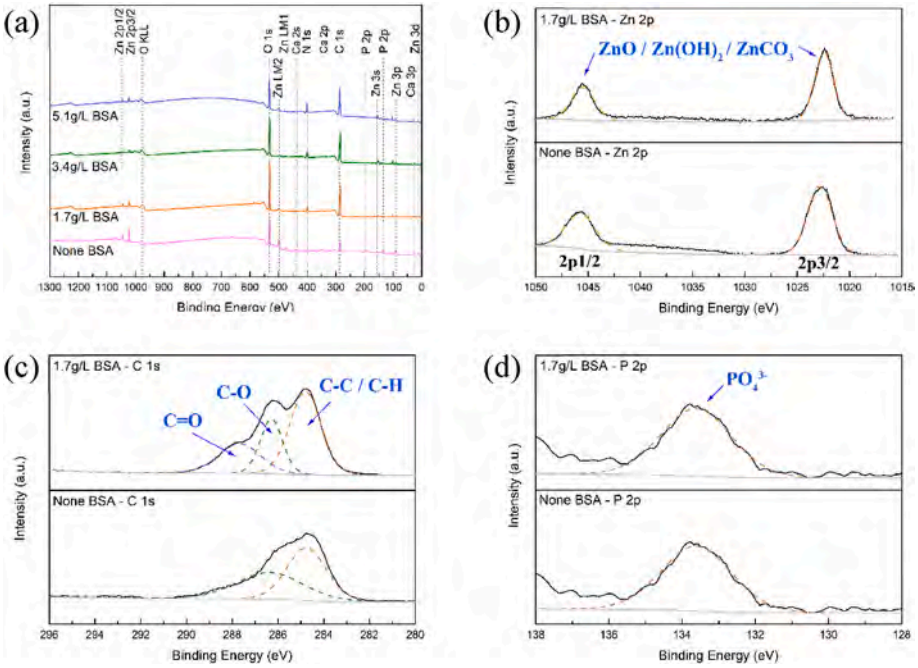

Fig. 8. XPS analysis of the Zn–Cu alloy immersed in Hanks' after 120 h. (a) XPS wide-scan spectra, High-resolution XPS spectra of (b) Zn 2p, (c) C 1 s, and (d) P 2p for different samples.

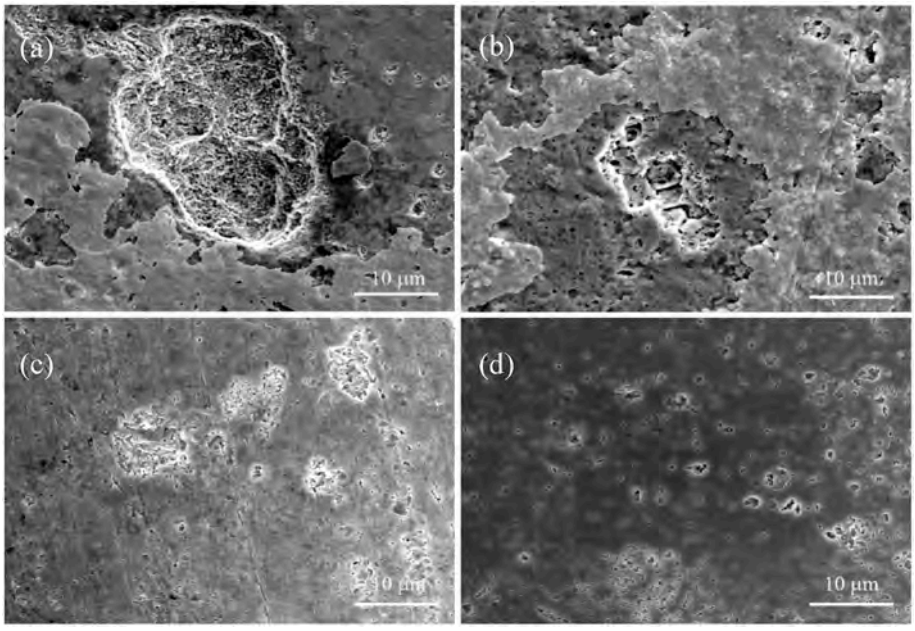

Fig. 9. Surface morphology of the Zn–Cu alloy in Hanks' solution containing different concentrations of BSA: (a) No BSA, (b) 1.7 g L^{-1} BSA, (c) 3.4 g L^{-1} BSA, and (d) 5.1 g L^{-1} BSA.

$ZnCO_3$ and phosphate compounds.

Fig. 9 shows the surface morphology after removing the corrosion products. The surface of the sample without BSA exhibits pitting corrosion and the corrosion pits are fairly obvious. After adding BSA, the pit diameter decreases and corrosion tends to proceed uniformly. When the BSA concentration is 5.1 g L^{-1}, there were no obvious large corrosion pits and corrosion is relatively uniform as well.

3.2. Electrochemical assessment

Fig. 10 shows the time-dependent EIS data of the Zn–Cu samples in Hanks' solution containing different concentrations of BSA under dynamic flowing conditions. The diameter of the capacitive arc of the sample without BSA decreases with immersion time and tends to be saturated. The corrosion products begin to form on the surface and the deposition and decomposition process is relatively stable. In the early stage of corrosion (0–48 h), with increasing BSA concentrations, the diameter of the capacitive loop decreases rapidly because adsorption retards the corrosion rate. In the later stage, owing to formation of the product layer and enrichment of corrosive ions in a stable state, the diameter of the capacitive loop tends to be consistent.

The polarization resistance (R_p), which depicts the kinetics of the

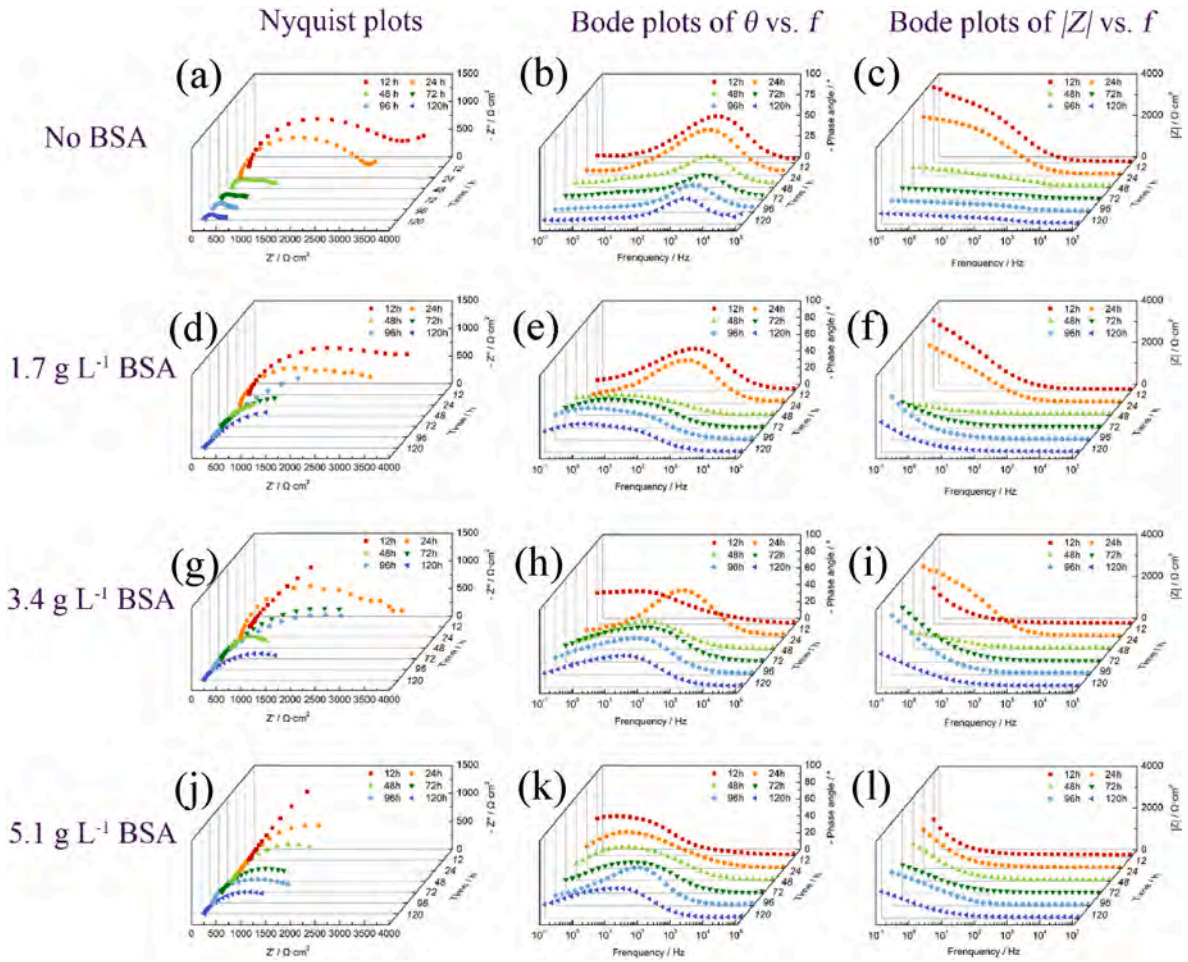

Fig. 10. EIS results of the Zn–Cu alloys at different time: (a–c) No BSA, (d–f) 1.7 g L^{-1} BSA, (g–h) 3.4 g L^{-1} BSA, and (j–k) 5.1 g L^{-1} BSA.

process, is derived from the EIS data by fitting it using the ZSimpwin software in accordance with the equivalent circuit depicted in Fig. 11. R_p shows a general decreasing trend during the immersion process, demonstrating that the protective effects of the corrosion product layer exceed the damaging effects of the corrosive ions. The polarization resistance increases with the addition of BSA in comparison to the case without BSA, demonstrating that BSA reduces the corrosion rate of the alloy. For different BSA concentrations, the polarization resistance is similar, with R_p increasing with higher BSA concentration during the first 48 h of immersion due to BSA adsorption. As the immersion time is extended (72–120 h), a protective film is formed on the surface of the material, the corrosion reaction tends to be stable dynamically.

4. Discussion

4.1. Corrosion rates of the Zn–Cu alloy

According to Tafel extrapolation, the corrosion potential (E_{corr}), corrosion current density (i_{corr}), anode Tafel constants (b_a) and cathode Tafel constants (b_c) are derived and presented in Table 2. In the absence of BSA, E_{corr} is the smallest indicative of highest corrosion. With increasing BSA concentration, i_{corr} increases, indicating that proteins inhibit corrosion of the Zn–Cu alloy and the inhibition effect decreases with increasing BSA consistent with the aforementioned corrosion morphology and characterization of the corrosion products. The linear polarization relationship between R_p and the corrosion current density i_{corr} (determined by R_p) can be expressed by the Stern formula [38]:

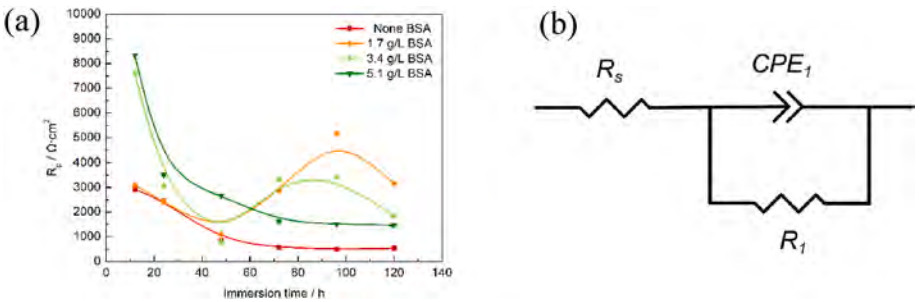

Fig. 11. Fitted results of Zn–Cu alloys during immersion for 120 h: (a) Change of the polarization resistance with time and (b) Equivalent electrical circuit.

Table 2
Electrochemical parameters of the Zn–Cu alloy after immersing.

Concentration of BSA (g·L^{-1})	E_{corr} (V)	i_{corr} (μA·cm^{-2})	b_a (mV)	b_c (mV)	CR (mm·y^{-1})
None	−1.03 ± 0.01	31.00 ± 0.93	167.35 ± 22.15	263.55 ± 19.11	0.46 ± 0.01
1.7	−1.15 ± 0.04	27.17 ± 1.32	101.62 ± 45.03	258.64 ± 40.31	0.41 ± 0.02
3.4	−1.13 ± 0.02	18.61 ± 1.15	101.22 ± 37.41	179.62 ± 26.56	0.29 ± 0.02
5.1	−1.12 ± 0.02	13.05 ± 1.09	68.93 ± 39.58	223.13 ± 28.01	0.20 ± 0.02

$$R_p = \frac{b_a b_c}{2.303(b_a + b_c) i_{corr}} . \quad (1)$$

Because the corrosion rate (CR, mm·y^{-1}) is proportional to i_{corr}, ASTM G59-97 can be used to determine the CR [39,40]:

$$CR = 8.76 \times 10^4 \frac{i_{corr} a}{NF\rho}, \quad (2)$$

where i_{corr} is the corrosion current density (A·cm^{-2}), a is the molar mass of the metal (65.324 g mol^{-1}), N is the number of electrons exchanged during the electrochemical reaction, F is Faraday's constant (26.8 Å·h), and ρ is the material density (g·cm^{-3}).

The change of corrosion rates of Zn–Cu alloy with immersion time is shown in Fig. 12. In the Hanks' solution without BSA, the corrosion rate increased significantly with the extension of time at first, and then leveled off, because of the formation of the surface film. The corrosion rate is significantly reduced in Hanks' solution after BSA was added, indicating that the protein inhibits corrosion. Due to the reaction between the corrosion ions in the solution and the Zn ions, the corrosion rate increased when 1.7 g L^{-1} BSA was added. The corrosion rate decreased as immersion time was increased because the BSA adsorbs on the sample's surface and prevents corrosion. At the later stage of corrosion, the corrosion product layer is unstable with the erosion of the flow field, and the release of Zn ions increased with the increase of immersion time, which enhanced the chelation effect and accelerated the corrosion rate. When the BSA content increased to 5.1 g L^{-1}, the corrosion rate becomes larger at the later stage of immersion because higher BSA concentration leads to the formation of more chelates.

According to the experimental results, there is an approximately linear relationship between CR of the alloy and CB (concentration of BSA) as shown in the following:

$$CR = \alpha \bullet CB + \beta \quad (3)$$

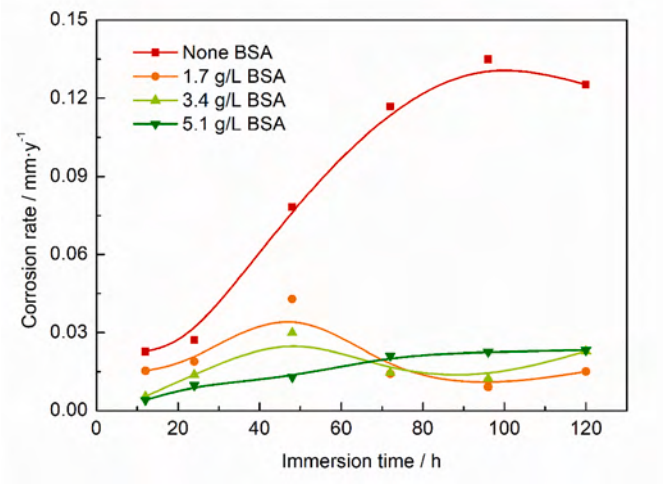

Fig. 12. CR variation calculated by EIS during immersion for 120 h.

The values of α and β vary with protein concentrations under flowing conditions and the fitted values for different BSA concentrations are listed in Table 3.

Fig. 13 shows the experimental results of CR and the fitted values in solutions with different CB in the early and later stages. There is a good agreement between the experimental and fitted results. CR decreases rapidly in the initial stage and then slows down with time extended due to dominant BSA adsorption in the beginning (0–48 h). As the BSA concentration rises up, adsorption increases and corrosion rates decrease. After 72 h, CR begins to increase slowly, indicating that the binding mechanism between BSA and the surface is no longer dominated by adsorption and protein chelation promotes further corrosion. All in all, the corrosion rates tend to be stable after formation of the surface film.

According to Fig. 13 and Table 3, the corrosion properties of the Zn–Cu alloy are determined. In the first 48 h, CR decreases rapidly indicating commencement of corrosion on the surface but BSA adsorption hinders corrosion at the same time. As time elapses, a large number of metallic ions are released to react with BSA to form chelates to promote CR. In the later stage, CR is stable dynamically indicative of dynamic equilibrium between corrosion and deposition of corrosion products.

For different concentrations of BSA.

4.2. Corrosion mechanism

According to the experimental results, corrosion process of the Zn–Cu alloy can be divided into the following stages. Initially, the Zn–Cu alloy dissolves *via* the following reactions [36,41,42]:

$$Zn \rightarrow Zn^{2+} + 2e^- \quad (4)$$

$$O_2 + 2H_2O + 4e^- \rightarrow 4OH^- \quad (5)$$

$$Zn^{2+} + 2OH^- \rightarrow Zn(OH)_2 \quad (6)$$

$$Zn^{2+} + 2OH^- \rightarrow ZnO + H_2O \quad (7)$$

The stability of $Zn(OH)_2$ and ZnO is affected by chloride, carbonate \bicarbonate, and phosphate in the medium and compounds such as $Zn_3(PO_4)_2$ and $ZnCO_3$ are formed [43–45].

The effects of proteins on the alloy surface are quite complex. Protein adsorption impedes ion migration and reduces CR. However, the isoelectric point of BSA is lower than that of the Zn and therefore the protein molecules on the surface are exposed to negatively charged acidic functional groups, which chemically react with dissolved metallic ions to form chelates that stimulate corrosion and dissolution of the materials [33,46–48].

The overall CR of the alloy is smaller after protein addition, indicating that BSA adsorption retards corrosion of the alloy. When CB is low, CR varies over time showing that adsorption and chelation of BSA compete with each other. With increasing CB, the fluctuation magnitude decreases and CR increases, suggesting that protein chelation gradually becomes dominant in the corrosion mechanism [34,48–51].

Corrosion in Hanks' solution with different CB can be summarized as shown in Fig. 14. In the early stage, BSA mainly adsorbs onto the alloy surface electrostatically. The larger the CB, the higher is proteins

Table 3
Values of α and β under different conditions.

Corrosion time (h)	α	β
12	$-3.29\cdot10^{-3}$	$1.95\cdot10^{-2}$
24	$-2.68\cdot10^{-3}$	$2.33\cdot10^{-2}$
48	$-8.85\cdot10^{-3}$	$5.87\cdot10^{-2}$
72	$2.04\cdot10^{-3}$	$9.70\cdot10^{-3}$
96	$3.95\cdot10^{-3}$	$1.25\cdot10^{-3}$
120	$2.43\cdot10^{-3}$	$1.21\cdot10^{-2}$

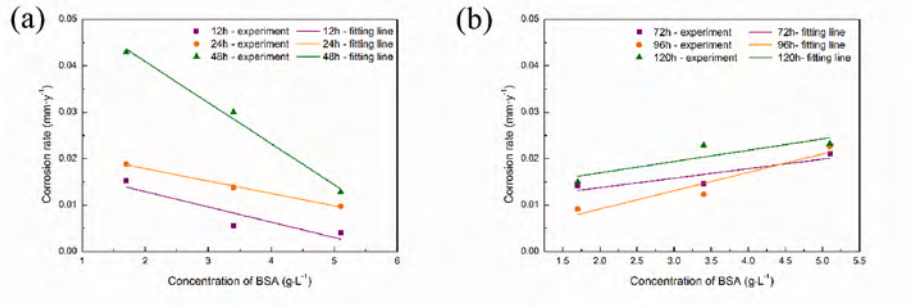

Fig. 13. Experimental results and quadratic fits of the *CR* of Zn–Cu alloy.

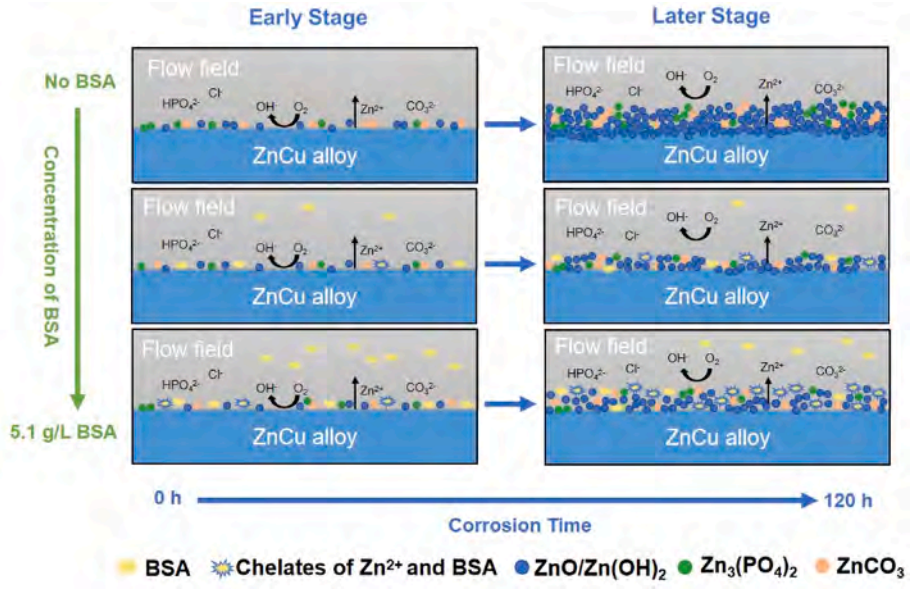

Fig. 14. Schematic diagram showing the effects of different concentrations of BSA on corrosion of the Zn–Cu alloy.

adsorption and the smaller is the surface area in contact with the solution, consequently giving rise to slower *CR*. The release of zinc ions during corrosion causes BSA to chelate with the metal cations to create metallic BSA chelates, which further encourage ion release and quicken corrosion. BSA shows chelation in the subsequent impregnation step to reduce the corrosion resistance. After deposition of corrosion products such as zinc oxide on the surface, by changing the surface state of the alloy and forming a protective surface film, *CR* stabilizes.

5. Conclusions

Corrosion behavior of the Zn–Cu alloy in Hanks' solution containing different concentrations of BSA is evaluated by analyzing the corrosion rate and degradation products. The results showed that.

(1) After 120 h of immersion, deep pits were evident on the surface of the sample, ZnO, $Zn(OH)_2$, $Zn_3(PO_4)_2$, and $ZnCO_3$ are the main corrosion products. Addition of BSA promotes the uniformity of corrosion and the chelation of BSA and metal cations enhances as the BSA content increases.

(2) Under the dynamic flowing conditions, BSA can prevent corrosion of the alloy, but higher concentrations of BSA will reduce the effectiveness of the prevention. The corrosion process can be divided into three stages. In the early stage of immersion, the electrostatic adsorption of BSA is strong, and the higher the concentration of BSA, the stronger the electrostatic adsorption, consequently reducing the corrosion rate. As the time of corrosion reaction increases, the release of zinc ions increases and BSA forms chelates with zinc ions. In this stage, a higher BSA concentration leads to the formation of more chelates and faster corrosion. Finally, after the deposition of corrosion products, a protective layer is formed and corrosion stabilizes.

(3) Via computer numerical simulation, a numerical model for the corrosion process of Zn–Cu alloy is established. In dynamic flowing conditions, the corrosion rates (*CR*) of Zn–Cu alloy and BSA concentrations (*CB*) of Hanks' solution matches a linear relationship of the formula $CR = \alpha \bullet CB + \beta$.

CRediT authorship contribution statement

Xin Zhang: Data curation, Validation, Investigation, Software, Writing, Experiments. **Lu Zhang:** Investigation, Software. **Dekang Zhang:** Experiments, Software. **Linyuan Han:** Conceptualization, Methodology. **Jing Bai:** Resources. **Zhihai Huang:** Resources. **Chao Guo:** Resources. **Feng Xue:** Supervision. **Paul K. Chu:** Supervision, Writing. **Chenglin Chu:** Conceptualization, Supervision, Project administration.

Declaration of competing interest

The authors declare that they have no known competing financial interests or personal relationships that could have appeared to influence

the work reported in this paper.

Data availability

Data will be made available on request.

Acknowledgements

This work was supported by the National Natural Science Foundation of China (grant numbers 52171236, 51971062), State Key Program of National Natural Science Foundation of China (Grant No. 52231005), Open Research Fund of Jiangsu Key Laboratory for Advanced Metallic Materials, Southeast University (grant number AMM2021A01), Post-graduate Research & Practice Innovation Program of Jiangsu Province (Grant No. KYCX20_0091), City University of Hong Kong Donation Research Grant (DON-RMG 9229021), City University of Hong Kong Strategic Research Grant (SRG 7005505), City University of Hong Kong Donation Grant (9220061), Hong Kong PDFS - RGC Postdoctoral Fellowship Scheme (PDFS2122-1S08 and CityU 9061014), Hong Kong HMRF (Health and Medical Research Fund) (2120972 and CityU 9211320).

References

[1] X. Tong, W. Cai, J. Lin, K. Wang, L. Jin, Z. Shi, D. Zhang, J. Lin, Y. Li, M. Dargusch, C. Wen, Biodegradable Zn−3Mg−0.7Mg2Si composite fabricated by high-pressure solidification for bone implant applications, Acta Biomater. 123 (2021) 407–417.
[2] F.D. Al-Shalawi, M.A.A. Hanim, M.K.A. Ariffin, C.L.S. Kim, D. Brabazon, R. Calin, M.O. Al-Osaimi, Biodegradable synthetic polymer in orthopaedic application: a review, Mater. Today: Proc. 74 (2023) 540–546.
[3] Y. Matsuda, M. Karino, T. Okui, T. Kanno, Complications of poly-l-lactic acid and polyglycolic acid (PLLA/PGA) osteosynthesis systems for maxillofacial surgery: a retrospective clinical investigation, Polymers-Basel 13 (2021) 889.
[4] Y. Zhao, W. Lu, A. Damgaard, Y. Zhang, H. Wang, Assessment of co-composting of sludge and woodchips in the perspective of environmental impacts (EASETECH), Waste Manage. (Tucson, Ariz.) 42 (2015) 55–60.
[5] Y.F. Zheng, X.N. Gu, F. Witte, Biodegradable metals, Mater. Sci. Eng. R Rep. 77 (2014) 1–34.
[6] L. Tan, X. Yu, P. Wan, K. Yang, Biodegradable materials for bone repairs: a review, J. Mater. Sci. Technol. 29 (2013) 503–513.
[7] Z. Wang, N. Li, R. Li, Y. Li, L. Ruan, Biodegradable intestinal stents: a review, Prog. Nat. Sci.: Mater. Int. 24 (2014) 423–432.
[8] S. Devgan, S.S. Sidhu, Evolution of surface modification trends in bone related biomaterials: a review, Mater. Chem. Phys. 233 (2019) 68–78.
[9] Y. Su, I. Cockerill, Y. Wang, Y. Qin, L. Chang, Y. Zheng, D. Zhu, Zinc-based biomaterials for regeneration and therapy, Trends Biotechnol. 37 (2019) 428–441.
[10] E. Mostaed, M. Sikora-Jasinska, J.W. Drelich, M. Vedani, Zinc-based alloys for degradable vascular stent applications, Acta Biomater. 71 (2018) 1–23.
[11] C. García-Mintegui, L.C. Córdoba, J. Buxadera-Palomero, A. Marquina, E. Jiménez-Piqué, M. Ginebra, J.L. Cortina, M. Pegueroles, Zn-Mg and Zn-Cu alloys for stenting applications: from nanoscale mechanical characterization to in vitro degradation and biocompatibility, Bioact. Mater. 6 (2021) 4430–4446.
[12] C. Wang, H.T. Yang, X. Li, Y.F. Zheng, Vitro evaluation of the feasibility of commercial Zn alloys as biodegradable metals, J. Mater. Sci. Technol. 32 (2016) 909–918.
[13] J. Cheng, B. Liu, Y.H. Wu, Y.F. Zheng, Comparative in vitro study on pure metals (Fe, Mn, Mg, Zn and W) as biodegradable metals, J. Mater. Sci. Technol. 29 (2013) 619–627.
[14] Y. Chen, W. Zhang, M.F. Maitz, M. Chen, H. Zhang, J. Mao, Y. Zhao, N. Huang, G. Wan, Comparative corrosion behavior of Zn with Fe and Mg in the course of immersion degradation in phosphate buffered saline, CORROS SCI 111 (2016) 541–555.
[15] P.K. Bowen, R.J. Guillory, E.R. Shearier, J. Seitz, J. Drelich, M. Bocks, F. Zhao, J. Goldman, Metallic zinc exhibits optimal biocompatibility for bioabsorbable endovascular stents, Mater. Sci. Eng. C 56 (2015) 467–472.
[16] B. Hennig, M. Toborek, C.J. Mcclain, Antiatherogenic properties of zinc: implications in endothelial cell metabolism, Nutrition 12 (1996) 711–717.
[17] S. Ahtzaz, M. Nasir, L. Shahzadi, W. Amir, A. Anjum, R. Arshad, F. Iqbal, A. A. Chaudhry, M. Yar, I.U. Rehman, A study on the effect of zinc oxide and zinc peroxide nanoparticles to enhance angiogenesis-pro-angiogenic grafts for tissue regeneration applications, MATER DESIGN 132 (2017) 409–418.
[18] M.A. Martinez Page, S. Hartmann, Experimental characterization, material modeling, identification and finite element simulation of the thermo-mechanical behavior of a zinc die-casting alloy, INT J PLASTICITY 101 (2018) 74–105.
[19] C. Zhou, H. Li, Y. Yin, Z. Shi, T. Li, X. Feng, J. Zhang, C. Song, X. Cui, K. Xu, Y. Zhao, W. Hou, S. Lu, G. Liu, M. Li, J. Ma, E. Toft, A.A. Volinsky, M. Wan, X. Yao, C. Wang, K. Yao, S. Xu, H. Lu, S. Chang, J. Ge, L. Wang, H. Zhang, Long-term in vivo study of biodegradable Zn-Cu stent: a 2-year implantation evaluation in porcine coronary artery, Acta Biomater. 97 (2019) 657–670.
[20] H. Li, H. Yang, Y. Zheng, F. Zhou, K. Qiu, X. Wang, Design and characterizations of novel biodegradable ternary Zn-based alloys with IIA nutrient alloying elements Mg, Ca and Sr, MATER DESIGN 83 (2015) 95–102.
[21] Z. Tang, H. Huang, J. Niu, L. Zhang, H. Zhang, J. Pei, J. Tan, G. Yuan, Design and characterizations of novel biodegradable Zn-Cu-Mg alloys for potential biodegradable implants, MATER DESIGN 117 (2017) 84–94.
[22] X. Tong, D. Zhang, X. Zhang, Y. Su, Z. Shi, K. Wang, J. Lin, Y. Li, J. Lin, C. Wen, Microstructure, mechanical properties, biocompatibility, and in vitro corrosion and degradation behavior of a new Zn–5Ge alloy for biodegradable implant materials, Acta Biomater. 82 (2018) 197–204.
[23] J. Venezuela, M.S. Dargusch, The influence of alloying and fabrication techniques on the mechanical properties, biodegradability and biocompatibility of zinc: a comprehensive review, Acta Biomater. 87 (2019) 1–40.
[24] X. Wang, X. Shao, T. Dai, F. Xu, J.G. Zhou, G. Qu, L. Tian, B. Liu, Y. Liu, In vivo study of the efficacy, biosafety, and degradation of a zinc alloy osteosynthesis system, Acta Biomater. 92 (2019) 351–361.
[25] Z. Shi, J. Yu, X. Liu, H. Zhang, D. Zhang, Y. Yin, L. Wang, Effects of Ag, Cu or Ca addition on microstructure and comprehensive properties of biodegradable Zn-0.8Mn alloy, Mater. Sci. Eng. C 99 (2019) 969–978.
[26] P. Trumbo, A.A. Yates, S. Schelicker, M. Poos, Dietary reference intakes Vitamin A, Vitamin K, Arsenic, Boron, Chromium, Copper, Iodine, Iron, Manganese, Molybdenum, Nickel, Silicon, Vanadium, and Zinc, J. Am. Dietetic Assoc. 101 (2001) 294–301.
[27] C.K. Sen, S. Khanna, M. Venojarvi, P. Trikha, E.C. Ellison, T.K. Hunt, S. Roy, Copper-induced vascular endothelial growth factor expression and wound healing, AM J PHYSIOL-HEART C 282 (2002) H1821–H1827.
[28] Z. Tang, J. Niu, H. Huang, H. Zhang, J. Pei, J. Ou, G. Yuan, Potential biodegradable Zn-Cu binary alloys developed for cardiovascular implant applications, J Mech. Behav. Biomed 72 (2017) 182–191.
[29] H. Ren, C. Pan, Y. Liu, D. Liu, X. He, X. Li, X. Sun, Fabrication, in vitro and in vivo properties of porous Zn–Cu alloy scaffolds for bone tissue engineering, Mater. Chem. Phys. 289 (2022), 126458.
[30] V.N. Tseluikin, Electrodeposition and properties of composite coatings modified by fullerene C60, Prot. Met Phys. Chem. 53 (2017) 433–436.
[31] V.N. Tseluikin, A.A. Koreshkova, Pulsed electrodeposition of composite coatings based on zinc–nickel alloy, Prot. Met Phys. Chem. 54 (2018) 453–456.
[32] M. Shourgeshty, M. Aliofkhazraei, A. Karimzadeh, Study on functionally graded Zn-Ni-Al_2O_3 coatings fabricated by pulse-electrodeposition, Surf. Eng. 35 (2019) 168–177.
[33] R. Hou, N. Scharnagl, R. Willumeit-Römer, F. Feyerabend, Different effects of single protein vs. protein mixtures on magnesium degradation under cell culture conditions, Acta Biomater. 98 (2019) 256–268.
[34] M. Talha, Y. Ma, P. Kumar, Y. Lin, A. Singh, Role of protein adsorption in the bio corrosion of metallic implants – a review, Colloids Surf. B Biointerfaces 176 (2019) 494–506.
[35] X. Liu, H. Yang, P. Xiong, W. Li, H. Huang, Y. Zheng, Comparative studies of Tris-HCl, HEPES and $NaHCO_3/CO_2$ buffer systems on the biodegradation behaviour of pure Zn in NaCl and SBF solutions, Corros. Sci. 157 (2019) 205–219.
[36] L. Liu, Y. Meng, A.A. Volinsky, H. Zhang, L. Wang, Influences of albumin on in vitro corrosion of pure Zn in artificial plasma, CORROS SCI 153 (2019) 341–356.
[37] L. Han, X. Li, J. Bai, F. Xue, Y. Zheng, C. Chu, Effects of flow velocity and different corrosion media on the in vitro bio-corrosion behaviors of AZ31 magnesium alloy, Mater. Chem. Phys. 217 (2018) 300–307.
[38] N.T. Kirkland, N. Birbilis, M.P. Staiger, Assessing the corrosion of biodegradable magnesium implants: a critical review of current methodologies and their limitations, Acta Biomater. 8 (2012) 925–936.
[39] R. Hou, R. Willumeit-Römer, V.M. Garamus, M. Frant, J. Koll, F. Feyerabend, Adsorption of proteins on degradable magnesium—which factors are relevant? ACS Appl Mater. Inter. 10 (2018) 42175–42185.
[40] ASTM G59-97, Standard Test Method for Conducting Potentiodynamic Polarization Resistance Measurements, ASTM, 2020.
[41] D. Hernández-Escobar, S. Champagne, H. Yilmazer, B. Dikici, C.J. Boehlert, H. Hermawan, Current status and perspectives of zinc-based absorbable alloys for biomedical applications, Acta Biomater. 97 (2019) 1–22.
[42] H. Yang, C. Wang, C. Liu, H. Chen, Y. Wu, J. Han, Z. Jia, W. Lin, D. Zhang, W. Li, W. Yuan, H. Guo, H. Li, G. Yang, D. Kong, D. Zhu, K. Takashima, L. Ruan, J. Nie, X. Li, Y. Zheng, Evolution of the degradation mechanism of pure zinc stent in the one-year study of rabbit abdominal aorta model, Biomaterials 145 (2017) 92–105.
[43] L. Li, H. Jiao, C. Liu, L. Yang, Y. Suo, R. Zhang, T. Liu, J. Cui, Microstructures, mechanical properties and in vitro corrosion behavior of biodegradable Zn alloys microalloyed with Al, Mn, Cu, Ag and Li elements, J. Mater. Sci. Technol. 103 (2022) 244–260.
[44] K. Törne, M. Larsson, A. Norlin, J. Weissenrieder, Degradation of zinc in saline solutions, plasma, and whole blood, J. Biomed. Mater. Res. B Appl. Biomater. 104 (2016) 1141–1151.
[45] A. Krężel, W. Maret, The biological inorganic chemistry of zinc ions, Arch. Biochem. Biophys. 611 (2016) 3–19.
[46] M. Höhlinger, D. Christa, V. Zimmermann, S. Heise, A.R. Boccaccini, S. Virtanen, Influence of proteins on the corrosion behavior of a chitosan-bioactive glass coated magnesium alloy, Mater. Sci. Eng. C 100 (2019) 706–714.
[47] R. Hou, F. Feyerabend, H. Helmholz, V.M. Garamus, R. Willumeit-Römer, Effects of proteins on magnesium degradation - static vs. dynamic conditions, J. Magnesium Alloys (2021). https://doi.org/10.1016/j.jma.2021.07.021.
[48] E. Jia, X. Zhao, Y. Lin, Z. Su, Protein adsorption on titanium substrates and its effects on platelet adhesion, Appl. Surf. Sci. 529 (2020), 146986.

[49] Y.L. Jeyachandran, E. Mielczarski, B. Rai, J.A. Mielczarski, Quantitative and qualitative evaluation of adsorption/desorption of bovine serum albumin on hydrophilic and hydrophobic surfaces, Langmuir 25 (2009) 11614–11620.

[50] D. Mei, C. Wang, S.V. Lamaka, M.L. Zheludkevich, Clarifying the influence of albumin on the initial stages of magnesium corrosion in Hank's balanced salt solution, J. Magnesium Alloys 9 (2021) 805–817.

[51] X. Liu, Y. Cheng, Z. Guan, Y. Zheng, Exploring the effect of amino acid and glucose on the biodegradation of pure Zn, CORROS SCI 170 (2020), 108661.